energies

MDPI

Article

Comparison of Star and String Offshore DC Collector Grid Topologies on the Aspect of Stability—An Impedance Approach

Matthias Biskoping [1,†], Tanmay Kadam [2,†], Sriram Karthik Gurumurthy [2,*,†] and Ferdinanda Ponci [2] and Antonello Monti [2]

[1] ABB Coroporate Research Center, 68526 Ladenburg, Germany; matthias.biskoping@de.abb.com
[2] Institute for Automation of Complex Power System, E.ON Energy Research Center, RWTH Aachen University, 52074 Aachen, Germany; tanmay.kadam@rwth-aachen.de (T.K.); fponci@eonerc.rwth-aachen.de (F.P.); amonti@eonerc.rwth-aachen.de (A.M.)
* Correspondence: sgurumurthy@eonerc.rwth-aachen.de
† These authors contributed equally to this work.

Abstract: Offshore Direct Current (DC) collector grids are a promising technology for decreasing the installation and operation costs of offshore wind parks. Nevertheless, the stability properties and hence the design of such DC collector grids is not common or standardised. Hence, this paper describes an attempt to fill these gaps by analysing the stability of two different types of DC collector grids—star and string—by considering identical operating conditions. The approach follows a non-parametric formulation of the impedance based Nyquist Stability Criterion. The hyperbolic Π equivalent formulation of the telegraph equation is adopted for modelling the submarine cable due to high capacitance that is distributed and thus the conventional 50 Hz Π-model is not sufficient anymore. Furthermore, the paper shows how to integrate the complex dynamics of wind turbines into the overall stability assessment through an impedance building algorithm. Finally, it is shown how to stabilise the collector grids by means of active control parameter changes and it has been observed that the star configuration of wind turbines is more favourable on account of stability and controllability.

Keywords: impedance based stability; MVDC grids; submarine cables; DC/DC converter; stability analysis; wind turbines; offshore grids

Citation: Biskoping, M.; Kadam, T.; Gurumurthy, S.K.; Ponci, F.; Monti, A. Comparison of Star and String Offshore DC Collector Grid Topologies on the Aspect of Stability—An Impedance Approach. *Energies* **2021**, *14*, 6253. https://doi.org/10.3390/en14196253

Academic Editor: Muhammad Ishaq Bhatti

Received: 29 July 2021
Accepted: 23 September 2021
Published: 1 October 2021

1. Introduction

The use of direct current (DC) in medium voltage (MV) distribution grids and high voltage (HV) transmission grids has significant advantages over the present day alternating current (AC) grid variants [1], mainly due to the increased capacity of existing cable infrastructure and compact conversion stations. Advancements in DC/DC power electronic converter topologies have enabled high efficiency and large power density compared to the AC counterpart [2]. Specific to the context of DC collector grids [1,3], the advantages include the elimination of redundant line filters, bulky transformers, compensators and output filters of wind turbine (WT), which leads to a reduced system size, reduced installation and maintenance cost [1,3]. High voltage DC (HVDC) is favoured when size of wind farms increases and when the distance from the shore is beyond 50 km [4,5]. The main argument against DC grids is its complex protection design which is constantly advancing; for example, fast converter shut down or multi-terminal DC breakers [6]. The overall stability of such DC collector grids in offshore wind farms is not standardised or established yet. This can be addressed by continued study and in-depth research. Detailed specifications for Medium Voltage DC (MVDC) shipboard power systems are currently available and this can be referred to as a benchmark common requirements for typical DC power system [7]. Further, the CIGRE working group 6.31 was established for investigating the needs and feasibility of building MVDC grids [8]. Their study concluded that MVAC and MVDC

systems are expected to be in coexistence for a significant time in future power systems. In particular, to facilitate the standardisation of MVDC grids, further studies involving advanced DC protection systems, various network topologies, simulation methods and tools for DC distribution systems must be promoted. This paper compares the stability between two of the common DC collector grid configurations—star and string—by considering identical system configuration and operating conditions. The paper shows how to stabilise such DC grids using active control through parameter variations.

The offshore medium voltage DC (MVDC) collector grid considered here consists of a number of wind turbines generating DC at their output and are typically arranged in configurations such as star or string. The generated power is transferred through submarine cables to an offshore platform hosting a DC/DC converter. This DC/DC converter steps up the voltage for further transmission via HVDC cables to the onshore grid.

Typically, the wind turbine dynamics are not considered in the impedance models in many research works such as [9–11]. In this paper, instead, an 11th order model for the WT is developed and presented in Section 4.1, wherein the proposed model is able to capture the impact of torque and the speed parameters in the impedance transfer function. The proposed WT model can capture low frequency dynamics as opposed to the models developed in [9–12]. This paper also models the closed-loop input impedance of the DC/DC converter considering a three phase Dual Active Bridge (DAB) topology. Submarine cables have high capacitance and it is distributed across the line and therefore the conventional lumped Π section models are not sufficient. Thus, the hyperbolic Π equivalent of a long-line model is adopted and modelled via its transmission matrix. Since analytical transfer functions cannot be obtained due to strong non-linearity, non-parametric impedance models are developed for submarine cables. A reduced order modelling for long lines is proposed in [13]; however, these models are based on S-parameter concept, which cannot be used to aggregate on a system level and furthermore these models do not consider the non-linear hyperbolic equations which are typical characteristics of submarine cables.

The stability of the collector grid depends not only on the standalone stability of individual components such as WTs and DC/DC converter but also their interconnection. Nyquist stability criterion (NSC) is a well known impedance-based method applied to DC systems and its extensions are available for AC systems [14,15]. NSC requires the analytical impedance transfer function of the source and load for its application. Furthermore, in the application of NSC, the presence of RHP poles or zeros in the individual source or load subsystem are typically neglected due to the assumption that every subsystem is standalone stable and non-minimum phase [14,15].

In reality, it is possible that the internal parameters of certain systems are not known or, due to the complex non-linearity involved, it may not be possible to derive linearised analytical transfer function. However, for such systems, the frequency response of individual subsystems can be extracted using wideband impedance measurement devices [16,17]. Thus, a black-box approach consisting of the impedance frequency response of individual subsystems can be used to determine the stability at the point of common coupling (PCC). Hence, a non-parametric NSC approach is applied wherein only the impedance frequency response data is required. It is proposed to first detect the unstable open loop poles from the frequency response of source and load impedance and then apply the non-parametric NSC [18] to avoid the conventional assumptions of neglecting RHP poles and zeroes. The calculation of non-parametric impedance can become tedious relying on circuit theory based reductions. Thus to formulate the impedance frequency response of the source and load, a non-parametric impedance building algorithm based on two-port network theory using the transmission matrix is developed. Through this algorithm, the complex dynamics of WTs, submarine cables and DC/DC converter can be integrated to form Thevenin equivalent non-parametric impedance models at the desired node where stability needs to be evaluated.

The major contributions of this work can be summarized as follows:

- An impedance-based modelling approach for off-shore WT systems, submarine cable and input impedance of three phase DAB;
- A non-parametric network impedance building algorithm based on two-port network theory via transmission matrices;
- Application of non-parametric impedance-based stability analysis for offshore DC collector grids;
- An effective comparison between star and string offshore WT typologies on the aspect of system stability.

2. Topologies of Offshore Wind Farms

For enabling comparability between star and string configurations, identical wind turbine parameters and cable parameters are used. The cable lengths are also identical as shown in Figures 1 and 2.

2.1. String

Figure 1 shows a schematic for interconnecting several WTs to a radial feeder forming a string. The number of WTs per string depends on the current carrying capacity of submarine cables and the capacity of individual generators. Many such strings are connected together at an offshore collector substation where it is transformed to higher voltages for onshore transmission [5]. The main advantage of this topology is its low installation cost. Moreover, the power ratings of the cable at the far end from the collector need not be high and hence can be designed accordingly. However, string topology lacks reliability. A fault in the string feeder will prevent the WTs behind the fault node from injecting power, which is often partially compensated for by a loop-back cable connecting one string to another [19].

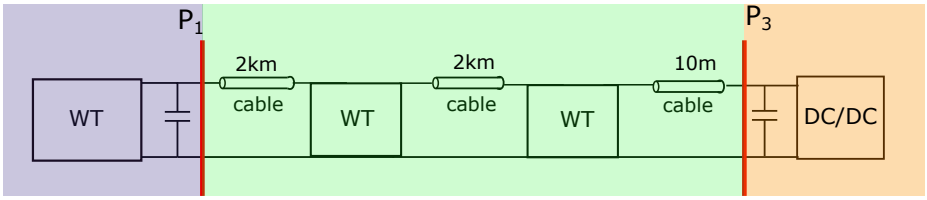

Figure 1. String configuration.

2.2. Star

In this configuration, each WT is connected to a common star point, as shown in Figure 2, through a submarine cable. Since every WT is connected to the star-point through a separate cable, the star topology provides high reliability and on the other hand the installation costs are higher due to increased cable lengths. However, the power ratings of the individual cables in the star are much lower compared to string topology.

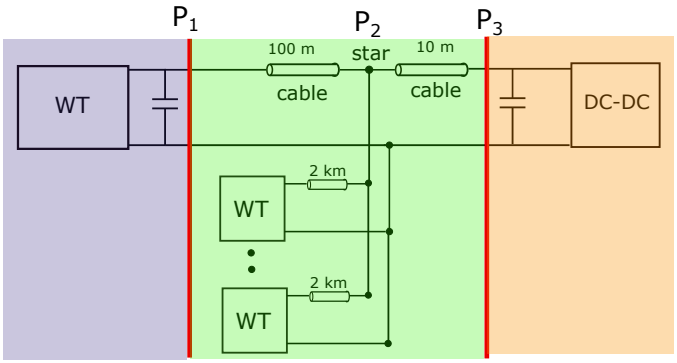

Figure 2. Star configuration.

3. Impedance Based Stability Criterion

According to the impedance-based stability criterion, the system under investigation is partitioned into the source and load subsystem where the subsystems can be represented either by Thevenin or Norton equivalent circuit [14]. The transfer functions of source and load subsystems are formulated by linearising the subsystems around a desired operating point and thus this linear representation is valid only for small signal studies [14]. Consider a small signal representation of the WT–MVDC collector grid model as shown in Figure 3, with WT represented by the current source in parallel with its output impedance Z_s and the collector grid model represented as an ideal voltage source in series with input impedance Z_l. The WT output current I in the Laplace domain can be written as:

$$I(s) = \left[I_s(s) - \frac{U_{\text{grid}}(s)}{Z_s(s)}\right] \cdot \frac{1}{1 + \frac{Z_l(s)}{Z_s(s)}}, \tag{1}$$

and the voltage U_{pcc} at the PCC can be written as:

$$U_{pcc}(s) = \left[I_s(s)Z_l(s) + U_{\text{grid}}(s)\right] \cdot \frac{1}{1 + \frac{Z_l(s)}{Z_s(s)}}. \tag{2}$$

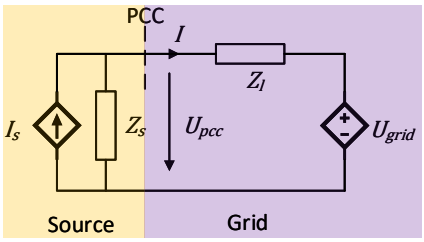

Figure 3. Small signal representation of source-grid model.

3.1. Nyquist Stability Criterion

The source-load interconnection is stable if the minor loop gain (MLG), which is the ratio of grid impedance Z_l to source impedance Z_s, satisfies the NSC. Let P be the number of RHP poles of the MLG (Z_l/Z_s) and N represent the number of anticlockwise (ACW) encirclements of the Nyquist plot of the MLG around critical point $-1 + j0$. Then the number of RHP poles of the closed loop system Z can be determined from (3). For a stable system, the number of ACW encirclements would equal the number of RHP poles of MLG, leading to a conclusion $Z = 0$.

$$N = P - Z. \tag{3}$$

3.2. Non-Parametric Nyquist Stability Criterion

Applying non-parametric NSC consists of four steps: Formulation of impedance ratio, identification of open loop RHP poles, identification of encirclements from the Nyquist plot and stability analysis. It is known that the NSC assumes that the open-loop transfer function is a proper function [18], which implies that the numerator has a lower degree than the denominator or the frequency response of the transfer function approaches zero at an infinite frequency. Therefore, the impedance ratio has been defined as a proper transfer function, formulated as MLG since $|Z_1| < |Z_2|$ at infinite frequencies [18].

$$\lim_{\omega \to \infty} \frac{Z_1}{Z_2} = 0. \tag{4}$$

The aforementioned terms (Z_1 and Z_2) have been deliberately used instead of Z_l and Z_s, as the impedance ratio of the system is not a fixed ratio in terms of Z_l/Z_s or Z_s/Z_l. Rather, the ratio would change depending upon the system interconnection and how the system is modelled (Thevenin or Norton equivalents). In case the analytical transfer

function is not known, Z_1 and Z_2 are chosen by observing the frequency response and checking the condition in (4) [18]. In practice, the frequency responses of the impedances are not available for frequencies tending infinity, hence the formulation of the impedance ratio is done from high frequency responses by the following conditions [18]:

- If the two impedances have different slope magnitudes at high frequency, the numerator impedance should be chosen as the one with smaller slope magnitude;
- If the two impedances have same slope magnitude at a high frequency, the numerator impedance should be chosen as the one with a smaller magnitude at high frequency.

Consider the ratio of impedances to be evaluated as Z_l/Z_s, the total number of RHP poles for this ratio is given by (5).

$$P_{\mathrm{RHP}}[Z_\mathrm{l}/Z_\mathrm{s}] = P_{\mathrm{RHP}}[Z_\mathrm{l}] + Z_{\mathrm{RHP}}[Z_\mathrm{s}]. \tag{5}$$

The presence of the RHP pole and RHP zero can be determined from the frequency responses of Z_l and Z_s respectively using the magnitude and phase behaviour of the system as shown in Figure 4 [18]. The number of ACW encirclements of critical point $-1 + \mathrm{j}0$ is identified by plotting the non-parametric Nyquist contour of Z_l/Z_s. The number of closed loop RHP poles can be determined by applying (3).

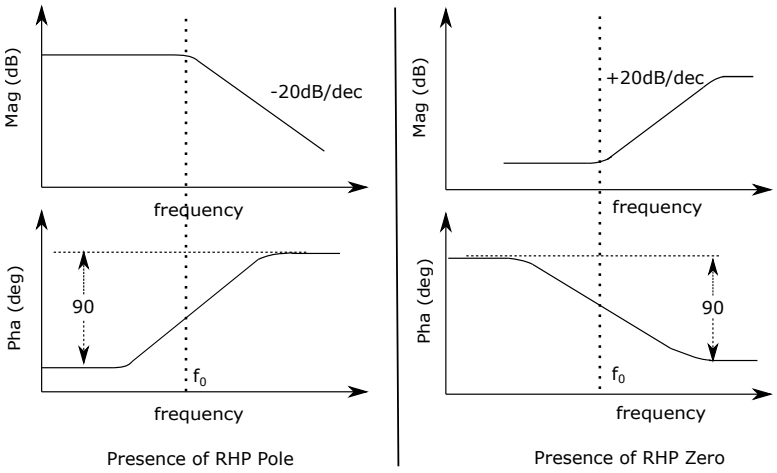

Figure 4. Frequency response of RHP poles and zeroes.

4. Impedance Modelling of the Interconnected System

Figure 5 represents a simplified offshore WT configuration, comprising of a single WT connected to an offshore DC/DC converter platform via submarine cables and this section performs the detailed modelling of the individual components.

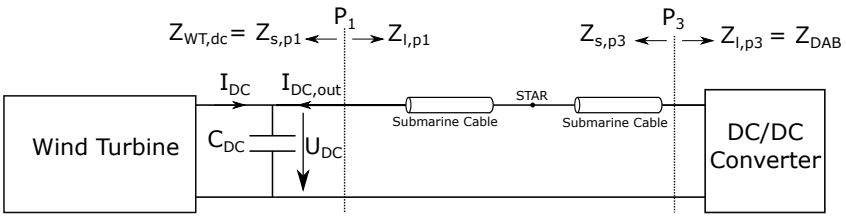

Figure 5. Single wind turbine interconnected system.

4.1. Model of the Wind Turbine System

The block diagram of the WT system is shown in Figure 6. This model is comprised of a wind turbine, a permanent magnet synchronous generator (PMSG), and a control system with an AC/DC converter. The blades of the wind turbine represent the mechanical turbine torque (T_{wt}) and angular speed (ω_{wt}) with which it rotates. The wind turbine has a nominal power rating of 5 MW, with a nominal speed ($\omega_{m,nom}$) of 12 rpm.

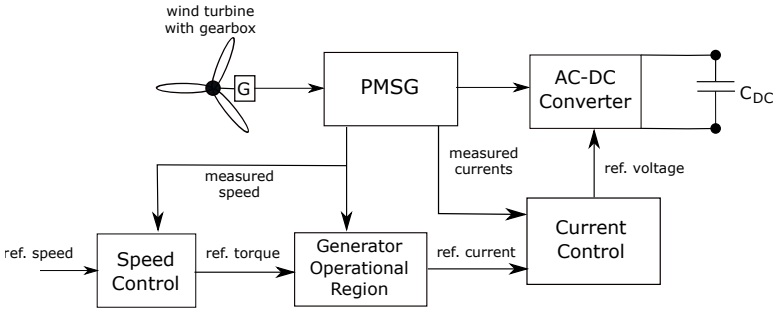

Figure 6. WT system.

4.1.1. PMSG

The wind turbine torque and speed are translated into equivalent machine level values through the gearbox. The PMSG has been modelled both electrically and mechanically. The electrical state space model has been created in such a way that it takes dq components of voltages ($U_{in,dq}$) as inputs with the disturbance function as $U_{dist,dq}$ and produces corresponding PMSG stator currents I_{dq}. These currents are used to compute the electromagnetic torque T_{em}, with respect to the torque equation [20].

$$T_{em} = \frac{3 \cdot p}{2} \cdot [\psi_{pm} \cdot I_q + (L_d - L_q) \cdot I_d \cdot I_q]. \tag{6}$$

The electrical model of PMSG has also been represented in the equivalent state space format as follows:

$$\dot{I}_d = -\frac{R}{L_d} I_d + \frac{\omega_m p L_q}{L_d} I_q + \frac{1}{L_d} U_{in,d} \tag{7}$$

$$\dot{I}_q = -\frac{R}{L_q} I_q - \frac{\omega_m p L_d}{L_q} I_d + \frac{1}{L_q} U_{in,q} - \frac{\omega_m p \psi_{pm}}{L_q}. \tag{8}$$

This electromagnetic torque then acts as an input to the mechanical model of PMSG, given by the state Equation (9) [20]:

$$\dot{\omega}_m = -D_{eq}\omega_m + \frac{1}{J_{eq}}(T_{em} - T_{wt}). \tag{9}$$

In Equations (6)–(9), ω_m denotes mechanical angular speed, p denotes the number of poles in PMSG, J_{eq} is the equivalent inertia of the (generator and wind turbine) system (in Kg m^2), D_{eq} is damping coefficient (in Kg m^2/s), ψ_{pm} is the permanent magnet flux linkage (in Wb), L_d,L_q are stator winding inductance along the dq axis (in H) and R is the stator winding resistance (in Ω).

4.1.2. Speed Control

The input to the speed controller is ω_{ref} (reference speed) and ω_m (mechanical turbine speed). ω_{ref} is pre-filtered and feed-forwarded to a tracking PI controller to produce the reference torque T_{ref}. The state equations representing the speed control are given by (10)–(13):

$$\dot{\omega}_{pf} = -\frac{\omega_{pf}}{\tau_{fs}} + \frac{\omega_{ref}}{\tau_{fs}} \tag{10}$$

$$\dot{T}_{ff} = -\frac{1}{\tau_{fs}} \tau_{ff} + \left(\frac{D_{eq}}{\tau_{fs}} - \frac{J_{eq}}{\tau_{fs}^2}\right)\omega_{ref} \tag{11}$$

$$\dot{\omega}_{int} = \omega_{pf} - \omega_m \tag{12}$$

$$T_{ref} = T_{ff} + \frac{J_{eq}}{\tau_{fs}}\omega_{ref} + K_p(\omega_{pf} - \omega_m) + K_i\omega_{int}. \tag{13}$$

Here, the pre-filtered speed ω_{pf}, feed-forward torque T_{ff} and ω_{int} represents system states and τ_{fs} represents the prefilter time constant.

4.1.3. Generator Operational Region

Depending upon T_{ref} and ω_m, the generator operational region block generates the command current ($I_{cmd,d}$ and $I_{cmd,q}$) for the current controller. These currents are calculated with respect to machine constraints (thermal, voltage and demagnetization constraints). The individual constraints are not explained here to avoid digression from the topic. Moreover, the individual operating zones have been previously analysed in detail in [21]. For application in wind generation systems, the PMSG operates along Maximum Torque per Ampere (MTPA) mode [20]. The MTPA control strategy ensures that, for a required torque, the minimum stator current is applied, which is a function of I_d and I_q for a given torque. This would in turn minimize the copper losses, which are proportional to the square of the current and the motor efficiency can then be improved.

The synthesis of command currents $I_{cmd,d}$ and $I_{cmd,q}$ pertaining to the MTPA mode can be found in [21].

4.1.4. Current Control

The current controller uses these command currents as inputs and produces reference voltages $U_{ref,d}$ and $U_{ref,q}$ as outputs. Similar to speed control, this scheme also uses prefilter, feedforward and PI control blocks for each d and q axis. The state equations representing the current control block are represented as follows:

$$\dot{I}_{pf,dq} = -\frac{I_{pf,dq}}{\tau_{fi}} + \frac{I_{cmd,dq}}{\tau_{fi}} \tag{14}$$

$$\dot{U}_{ff,dq} = -\frac{1}{\tau_{fi}} U_{ff,dq} + \left(\frac{R}{\tau_{fi}} - \frac{L_{dq}}{\tau_{fi}^2}\right) I_{cmd,dq} \tag{15}$$

$$\dot{I}_{int,dq} = I_{pf,dq} - I_{dq} \tag{16}$$

$$U_{ref,d} = K_{pdi}(I_{pf,d} - I_d) + K_{idi} I_{int,d} + U_{ff,d} + \frac{L_d}{\tau_{fi}} I_{cmd,d} - I_q L_q \omega_m p \tag{17}$$

$$U_{ref,q} = K_{pqi}(I_{pf,q} - I_q) + K_{iqi} I_{int,q} + U_{ff,q} + \frac{L_q}{\tau_{fi}} I_{cmd,q} + (I_d L_d + \psi_{pm})\omega_m p. \tag{18}$$

Here, τ_{fi} denotes the prefilter time constant, K_{pdi}, K_{idi}, K_{pqi}, K_{iqi} are proportional and integral gains (along d and q axes respectively).

$I_{pf,dq}$ (dq axis pre-filtered currents), $U_{ff,dq}$ (dq axis feed-forward voltages), and $I_{int,dq}$ represent system states. Command currents $I_{cmd,dq}$ and voltages $U_{ref,dq}$ forms inputs and outputs respectively. Current control is modelled using PMSG equations, which act as a plant for this control. Moreover, cross coupling between U_d and U_q is also considered while deriving the state space equivalent model of the current control system.

The entire control strategy discussed so far can be summarized in Figure 7, where highlighted variables $U_{dist,dq}$ and I_{dq} denote inputs and outputs, respectively. This forms a closed loop system, where the effects of disturbance voltages on output currents is formulated as an admittance transfer function defined as $Y_{WT,dq} = \frac{I_{dq}}{U_{dq}}$. Figure 8 shows the impact of torque on $Y_{WT,dq}$ when the WT speed ω_m is fixed to a nominal value.

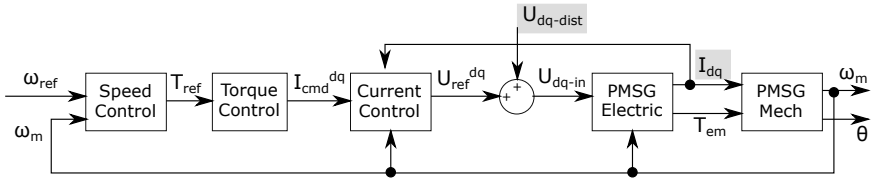

Figure 7. WT control block diagram.

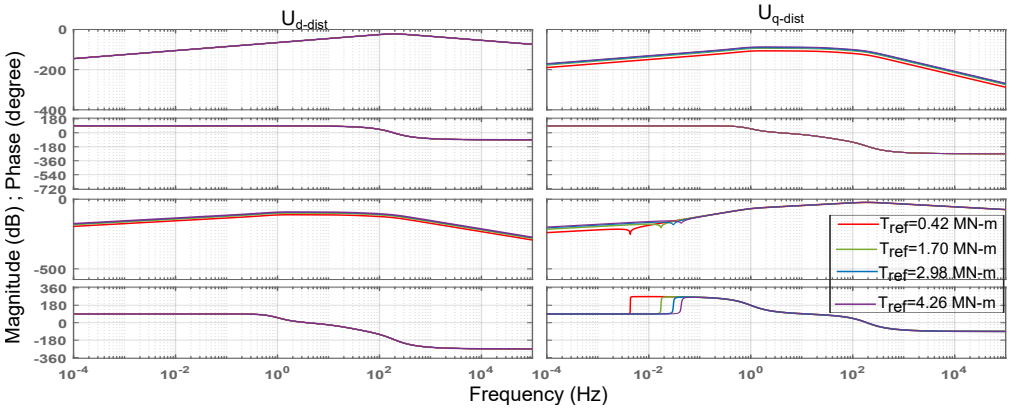

Figure 8. Admittance $Y_{WT,dq}$ with fixed ω_m and variable torque.

Referring to Figure 5, to study the stability of the system based on impedance, the DC impedance transfer function ($Z_{WT,dc}$) of the WT is required. To obtain $Z_{WT,dc} = \frac{U_{DC}}{I_{DC}}$, the AC/DC converter needs to be modelled in terms of equivalent equations. For simplicity, the power losses in the converter are neglected as defined in (19). The signs of I_d and I_q have been reversed considering the machine in generating mode. Since $P_{AC} = P_{DC}$, we have:

$$\frac{3}{2}(-U_d I_d - U_q I_q) = U_{DC} I_{DC}. \tag{19}$$

Using Figure 5, the DC impedance transfer function for the wind turbine control system can be derived. Here, U_{DC} is the output voltage as measured across capacitor C_{DC}. I_{DC} is the DC current output of WT and $I_{DC,out}$ is the DC current that is linked with further interconnection of this system. Hence, the DC impedance transfer function would be:

$$Z_{WT,dc} = \frac{U_{DC}}{I_{DC,out}}. \tag{20}$$

The state equation of the capacitor voltage can be written using (19):

$$\dot{U}_{DC} = \frac{1}{C_{DC}}\left[\frac{3}{2}(-U_d I_d - U_q I_q)\frac{1}{U_{DC}} + I_{DC,out}\right]. \tag{21}$$

In (21), terms U_d and U_q are the control variables of the current controller. These get disturbed by voltage fluctuations of U_{DC} which are modelled by $U_{dist,dq}$. The transfer function is built by incorporating the converter modulation index and the $U_{ref,dq}$ participation factor on the overall length of the combined vector U_{ref} so that the disturbance would consider any perturbation on the DC side of the system. This is achieved by (22), which is used to reflect any disturbance on the DC side onto the AC side dq axis voltage components.

$$U_{dist,dq} = \underbrace{\frac{U_{ref,dq}}{U_{ref}}}_{\text{dq part.}} \cdot \underbrace{\frac{U_{ref}}{U_{DC,ref}/2}}_{\text{mod. index}} \cdot (U_{DC} - U_{DC,ref}). \tag{22}$$

Here, $U_{ref} = \sqrt{U_{ref,d}^2 + U_{ref,q}^2}$ and $U_{DC,ref}$ is the reference DC voltage across the output capacitor C_{DC}. These dq disturbance functions get added to voltage components

U_{dq}, acting as inputs to the PMSG machine. The overall state system is thus derived, with input as $I_{DC,out}$ and output as U_{DC}, to obtain the impedance transfer function of a wind turbine system at a given operating point.

The validity of the transfer function given in (22) is checked using Matlab/Simulink and PLECS via the configuration in Figure 9.

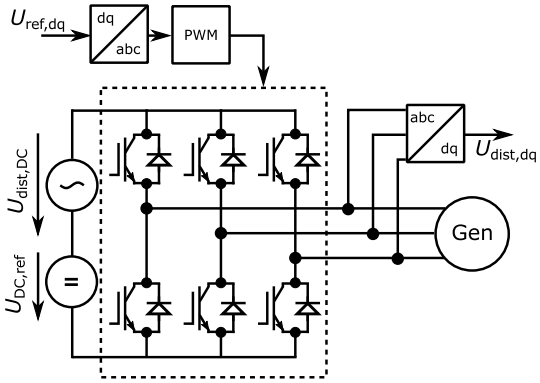

Figure 9. Implementation in Matlab/Simulink using PLECS for evaluation of U_{dq} transfer function.

The frequency and excitation on the DC-bus is given by $U_{dist,DC} = 100\ V \cdot \sin(2\pi \cdot 600\ Hz \cdot t)$ and the simulated result can be seen in Figure 10, which conforms the transfer function from (22), as can be seen by the spectral value at 600 Hz. The requested $U_{ref,dq}$ can be read at zero frequency in the spectrum. The spectral parts around 2000 Hz are related to the switching frequency, which is not considered in this paper.

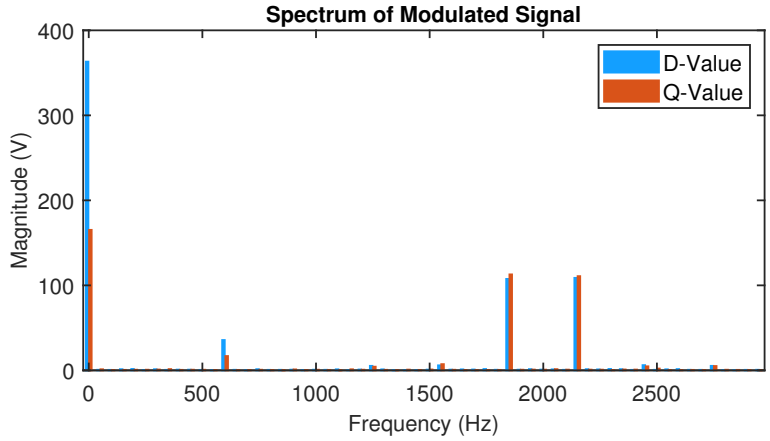

Figure 10. Spectrum of $U_{dist,dq}$.

A simulation model in Matlab/Simulink using the PLECS-Toolbox from Plexim is represented for the power electronic and machine part as shown in Figure 11. In Figure 12, the Bode response of impedance function Z_{DC} of the wind turbine system is plotted for two cases, when the wind turbine is operating at nominal torque and $\omega_{m,nom}$, thereby producing nominal power and when wind turbine is producing minimum power. The theoretical transfer function as seen in Figure 12 has been evaluated against the simulink model from Figure 11. The transfer function from the simulation behaves exactly the same as shown by the "O" points in the graph.

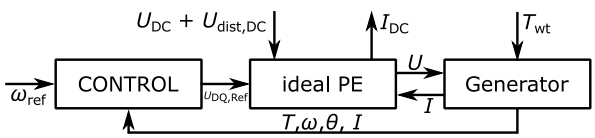

Figure 11. Simulation implemented in Matlab/Simulink using PLECS.

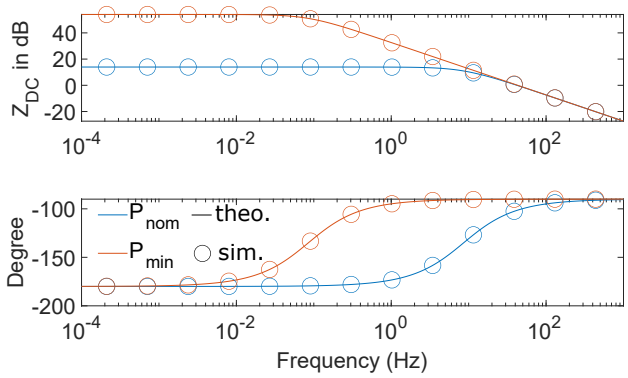

Figure 12. Wind Turbine Z_{DC} Response at Nominal and Minimum Power.

4.2. Modelling of Submarine Cables

Submarine cables are typically designed to have low resistance and thus low losses but they have high capacitance, which is distributed across the length of the line (l) and thus cannot be neglected. In this paper, the high frequency effects on cables resistance due to skin and proximity effects are neglected, cable parameter dependencies on ageing and temperature are also neglected. The cable parameters used for the analysis are $R^{'} = 0.0991\ \Omega/\text{km}$, $L^{'} = 0.33\ \text{mH/km}$ and $C^{'} = 0.46\ \mu\text{F/km}$. Long line Π-section model as shown in Figure 13 is adopted to define impedance (Z_c) and admittance (Y_c) of the cable in terms of characteristic impedance (Z_w) and propagation constant (γ) as given by (23) and (24). The characteristic impedance is defined as $Z_w = \sqrt{(R' + j\omega L')/(j\omega C')}$ and the propagation constant is defined as $\gamma = \sqrt{(R' + j\omega L')(j\omega C')}$. Using these equations, the parameters of the Π-section components are obtained at every frequency.

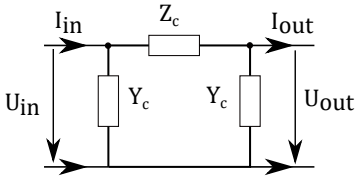

Figure 13. Π-section model of submarine cable.

$$Z_c = Z_w \cdot \sinh \gamma \cdot l \tag{23}$$

$$Y_c = \frac{\tanh \gamma \cdot l/2}{Z_w}. \tag{24}$$

The relation between sending and receiving end for each element can be modelled via transmission matrices (25), which allows us to easily combine the different elements to receive the needed structure for impedance analysis.

$$\begin{bmatrix} U_{in} \\ I_{in} \end{bmatrix} = \begin{bmatrix} 1 + Z_c Y_c & Z_c \\ 2Y + Z_c Y_c^2 & 1 + Z_c Y_c \end{bmatrix} \begin{bmatrix} U_{out} \\ I_{out}. \end{bmatrix} \tag{25}$$

4.3. Modelling of DC/DC Converter

The DC/DC converter acts as a collecting platform for a number of offshore wind turbines connected in a certain topology. The DAB topology is well suited for such applications due to its galvanic isolation and high efficiency due to inherent soft switching capability [11,22]. A typical three phase configuration of DAB is shown in Figure 14. The power transferred (P_{DAB}) from the primary to the secondary side is a function of the

phase shift angle between the PWM signals of the primary and secondary sides and it is given by (26) [22].

$$P_{DAB} = \frac{U_{in}^2 d\phi}{\omega_s L_s n_t}\left(\frac{2}{3} - \frac{\phi}{2\pi}\right). \tag{26}$$

Here, $d = U_{out}/U_{in}$ is the dynamic voltage conversion ratio and f_s $(= \omega_s/2\pi =$ 1 kHz) is the switching frequency. Voltages U_{in} and U_{out} are at 5 kV and 100 kV respectively. The power transfer is also dependent on the leakage inductance L_s and it is a design parameter such that maximum power is achieved for $\phi \leq \pi/6$ such that reactive power in the AC link is minimized. The state equation of DAB at the input capacitor can be written as (27):

$$\dot{U}_{in} = \frac{1}{C_{in}}\left[I_{in} - \frac{U_{in}\phi}{\omega_s L_s n_t}\left(\frac{2}{3} - \frac{\phi}{2\pi}\right)\right]. \tag{27}$$

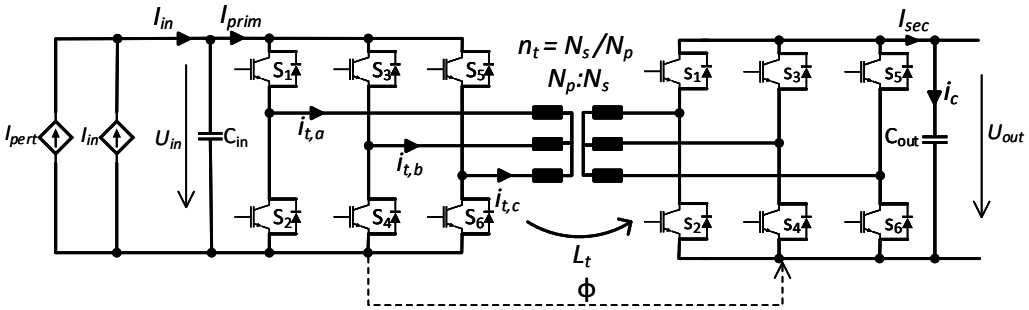

Figure 14. Dual Active Bridge.

The DC/DC converter is designed to control the input side DC voltage to a given reference set-point. Thus, a PI control with gains $K_{p,DC}$ and $K_{i,DC}$ is to control the required phase shift ϕ to be used in (27).

$$\phi = K_{p,DC}(U_{in} - U_{DC,ref}) + K_{i,DC}x_d. \tag{28}$$

The state equation introduced by the controller is:

$$\dot{x}_d = U_{in} - U_{DC,ref}. \tag{29}$$

From (27)–(29), the state space equivalent of the DC/DC converter system can be formulated with input as I_{in} and output as U_{in} such that the closed-loop input impedance is obtained as (30):

$$Z_{DAB} = \frac{3L_s n_t \omega_s \pi s}{3\pi C_{in} L_s n_t \omega_s s^2 + (K_{p,DC}s + K_{i,DC})U_g\beta}, \tag{30}$$

where $\beta = 2\pi - 3K_{i,DC}x_d + 3K_{p,DC}(U_{dc,ref} - U_{in})$.

The closed loop input impedance model of the three phase DAB is validated in SIMULINK through switched models. By applying a sinusoidal perturbation current of 10 percent superimposed over the nominal WT DC current, the input DC link voltage is perturbed depending on the closed loop input impedance of the converter. By using the recursive Fourier transform method [11], the frequency dependent impedance is extracted. Since the three phase DAB is a non-linear system, the impedance model is validated at different power levels. Considering a power level of 100 MW as the maximum rated capacity of the converter, the impedance model is validated for 100 MW, 50 MW and 5 MW operating point. Figures 15 and 16 compare the developed theoretical impedance model with the data obtained from simulations. It can be observed that the linearized model is in close agreement with the simulated data for various power levels. Since the averaged model is only accurate up to switching frequency, the deviation in the magnitude response could be observed close to the switching frequency. However, these frequencies are not

critical since the DC link voltage stability is of primary concern in this paper, which occur at much lower frequencies.

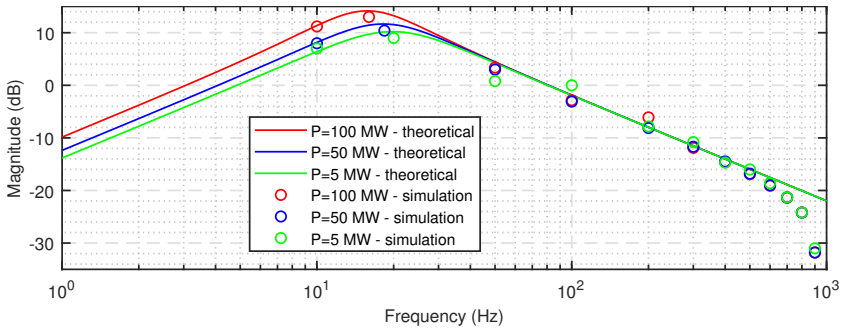

Figure 15. DAB Impedance Magnitude Validation.

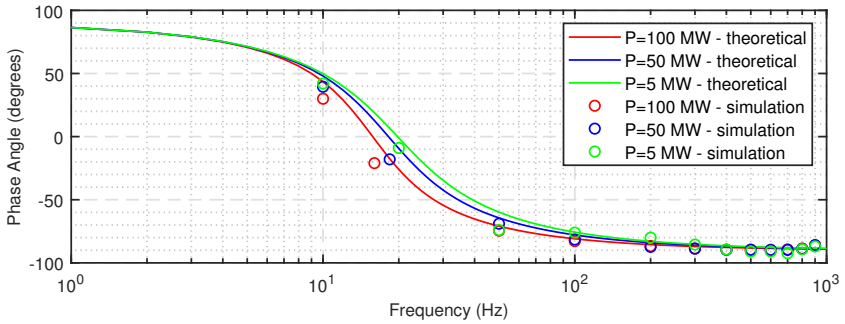

Figure 16. DAB Impedance Phase Angle Validation.

5. Non-Parametric Impedance Building Algorithm

In this section, an impedance building algorithm is described to construct the overall impedance required using two-port network theory. A star configuration of the offshore wind-farm is presented in Figure 17, wherein the equivalent impedance of the wind-turbines connected at the star point through the submarine cables are $Y_{s1} \cdots Y_{sn}$. As an example, let us consider the stability analysis at P_1 in Figure 17, then the impedance $Z_{l,p1}$ is required. The algorithm starts from the break away point P_1 and traverses through the network and two types of basic elements are encountered: shunt or series. Shaded section *a* in Figure 18 represents shunt element and transmission matrix is given by (31).

$$\begin{bmatrix} U_{in} \\ I_{in} \end{bmatrix} = \begin{bmatrix} 1 & 0 \\ Y_{c1} & 1 \end{bmatrix} \begin{bmatrix} U_1 \\ I_1. \end{bmatrix} \tag{31}$$

The next shaded section *b* in Figure 18 contains a series element and the transmission matrix is given by (32):

$$\begin{bmatrix} U_1 \\ I_1 \end{bmatrix} = \begin{bmatrix} 1 & Z_{c1} \\ 0 & 1 \end{bmatrix} \begin{bmatrix} U_2 \\ I_2. \end{bmatrix} \tag{32}$$

Thus, the overall impedance can be obtained by multiplying the respective transmission matrices of every individual shunt and series element until the end element which closes the loop, that is Z_{DAB}.

$$\begin{bmatrix} U_{in} \\ I_{in} \end{bmatrix} = \underbrace{\begin{bmatrix} 1 & 0 \\ Y_{c1} & 1 \end{bmatrix} \begin{bmatrix} 1 & Z_{c1} \\ 0 & 1 \end{bmatrix} \cdots}_{\begin{bmatrix} A_{eq} & B_{eq} \\ C_{eq} & D_{eq} \end{bmatrix}} \begin{bmatrix} U_{out} \\ I_{out}. \end{bmatrix} \tag{33}$$

Since $U_{out} = Z_{DAB} I_{out}$, (33) can be be used to calculate the non-parametric impedance $Z_{l,p1}$ as:

$$Z_{l,p1}(j\omega_i) = \frac{U_{in}}{I_{in}} = \frac{A_{eq} Z_{DAB} + B_{eq}}{C_{eq} Z_{DAB} + D_{eq}}, \tag{34}$$

where ω_i represents the frequency of interest within the interval $-\omega_{max} \leq \omega_i \leq \omega_{max}$. The shunt elements at the star-point $Y_{s1} \cdots Y_{sn}$ can also be reduced using the impedance building algorithm. The corresponding equivalent circuit of the star-sections are shown in Figure 19. The port variables can be written using the transmission matrix as shown in (35).

$$\begin{bmatrix} U_s \\ I_s \end{bmatrix} = \underbrace{\begin{bmatrix} 1 & 0 \\ Y_c & 1 \end{bmatrix} \begin{bmatrix} 1 & Z_c \\ 0 & 1 \end{bmatrix} \cdots}_{\begin{bmatrix} A_s & B_s \\ C_s & D_s \end{bmatrix}} \begin{bmatrix} U_{wt} \\ I_{wt}. \end{bmatrix} \tag{35}$$

The element that closes the loop is $Z_{WT,dc} = U_{wt} / I_{wt}$. Thus, the star-point admittance can be calculated as:

$$Y_s(j\omega_i) = \frac{I_s}{U_s} = \frac{C_s Z_{WT,dc} + D_s}{A_s Z_{WT,dc} + B_s}, \tag{36}$$

where A_s, B_s, C_s and D_s are the equivalent elements of the transmission matrix representing the star-section. Thus, the proposed method can calculate the non-parametric Thevenin equivalent impedance for the defined frequency range. Through this method, complex circuit theory based reductions can be avoided.

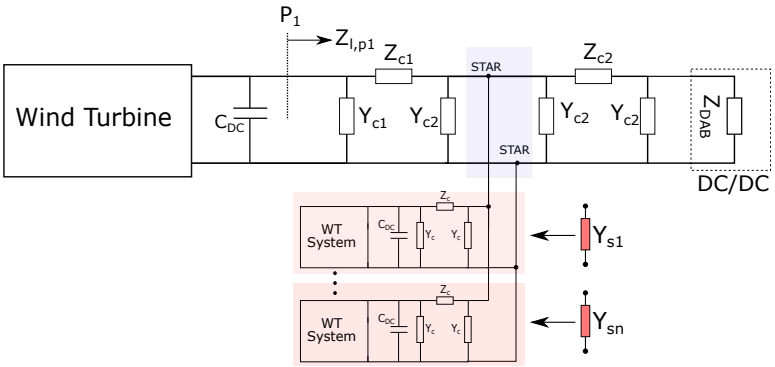

Figure 17. Multiple wind turbines in star configuration.

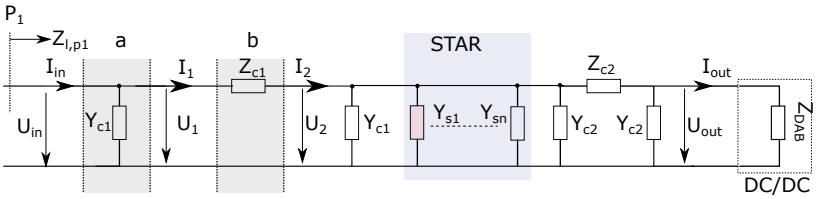

Figure 18. Equivalent model of the star connected offshore DC grid as seen from point P_1.

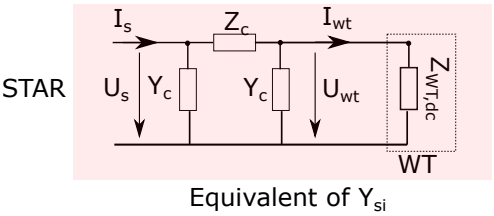

Figure 19. Equivalent model of a WT connected to the Star point through a submarine cable .

6. Frequency Domain Stability Analysis

Nominal and identical operating conditions are chosen for every WT. As explained in Section 2, all the parameters are chosen identically to enable comparability between Star and String topologies. Pertaining to Section 5, the frequency grid chosen for the calculation of non-parametric impedance is from −10 kHz to 10 kHz with a resolution of 1 Hz. For the Nyquist plots produced, the positive frequency part is represented as solid lines and the negative frequency part as dashed lines. The stability analysis of every case presented in this section considers the variation in DC/DC converter control gains, WT control parameters, WT output capacitance, input capacitance of DAB and submarine cable and only the significant results are presented.

6.1. Stability Analysis of Single Wind Turbine

Consider a single WT feeding power to a DC/DC converter as shown in Figure 5. The system stability is checked by applying the non-parametric NSC at the point P_1 which is the terminal of WT. The stability of this system can be determined by carefully analysing the Bode and Nyquist plots of the two impedances involved, namely $Z_{s,p1}$ and $Z_{l,p1}$ representing closed-loop WT impedance and load impedance (submarine cable + DAB), respectively.

Figure 20 illustrates the frequency response of $Z_{s,p1}$ and $Z_{l,p1}$. Unlike conventional NSC, analytical transfer functions are not available but rather frequency response data. In non-parametric NSC, the MLG is chosen by observing the high frequency response. At high frequencies, the magnitude of $Z_{s,p1} < Z_{l,p1}$ and it can be inferred that the ratio will tend to zero at infinite frequency. Thus, the stability is checked by evaluating the RHP poles of the MLG $Z_{s,p1}/Z_{l,p1}$. The total number of RHP poles in this case would be the sum of RHP poles of $Z_{s,p1}$ and RHP zeroes of $Z_{l,p1}$. It can be observed from the shaded portion of Figure 20 that $Z_{s,p1}$ has one RHP pole since there is a $+90°$ change in phase for -20 dB/dec change in magnitude, whereas $Z_{l,p1}$ has no RHP zeroes. The Nyquist plot of $Z_{s,p1}/Z_{l,p1}$ is plotted in Figure 20, where there is one ACW encirclement and thus the system is stable. The stability of the same system is now evaluated at P_3 as shown in Figure 5. Figure 21 illustrates the frequency responses of two impedances $Z_{s,p3}$ and $Z_{l,p3}$. Note that, at high frequencies, the magnitude of $Z_{s,p3} > Z_{l,p3}$, thus the ratio to be investigated, is $Z_{l,p3}/Z_{s,p3}$.

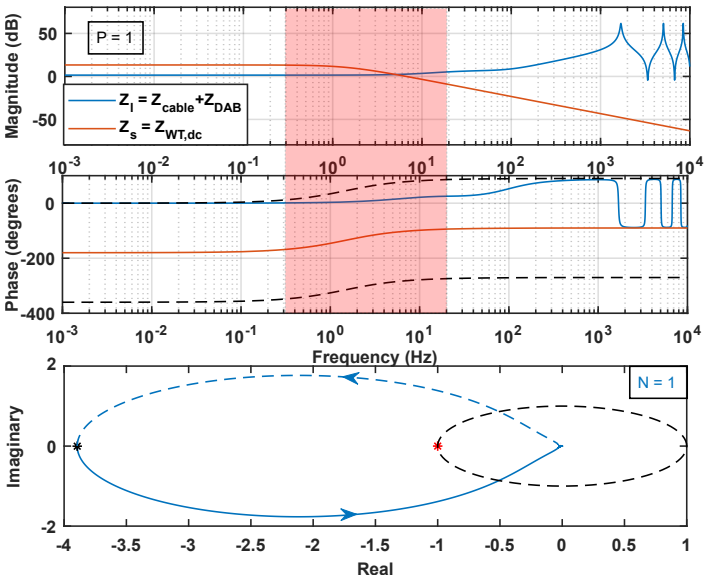

Figure 20. Stability Analysis for Single WT at P_1.

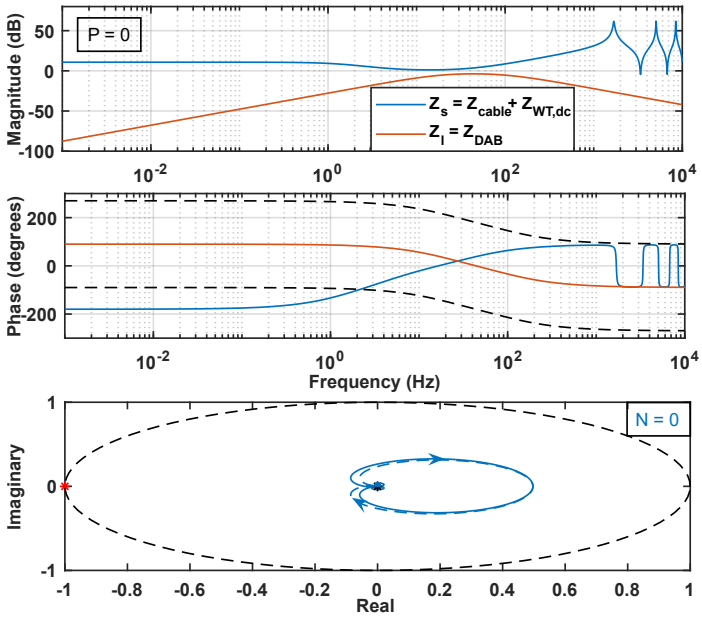

Figure 21. Stability Analysis for Single WT at P_3.

From the Bode plots in Figure 21, it is clear that Z_l and Z_s do not have RHP pole and RHP zero respectively and thus no open loop unstable poles. Moreover, the Nyquist plot of $(Z_{l,p3}/Z_{s,p3})$ yields no encirclements around the critical point observed in Figure 21, which is well within the unit circle. This shows that the system is stable at the DC/DC converter side interconnection. Similar analysis has been carried out to check the stability of the system for effects on the variation in DC/DC converter gains, submarine cable parameters and also wind turbine control system parameters.

To demonstrate the effects of variation in DC/DC converter gains on the stability of single WT system, Bode and Nyquist plots were obtained in the similar fashion. The gains (K_p and K_i) were reduced in steps so as to observe the corresponding system behaviour. The frequency response of this system in terms of Bode indicated one RHP pole ($P = 1$ in Nyquist Equation (3)) for the corresponding variation in gains. The Nyquist plots, as the controller gains are reduced, are illustrated in Figure 22. As can be observed, stable curves in Figure 22 are encircling the critical point in the ACW direction; however, as the gains are reduced, the curve tends to shift towards instability. Once the gains are reduced beyond a threshold, a CW encirclement (black coloured curve) around the critical point can be seen. For the system to be stable, it should have one ACW encirclement ($N = 1$) around the critical point and no closed loop RHP poles. For the system indicated with the black curve, $N = -1$ as per the Nyquist equation. This shows that the system has closed loop RHP poles, leading to instability.

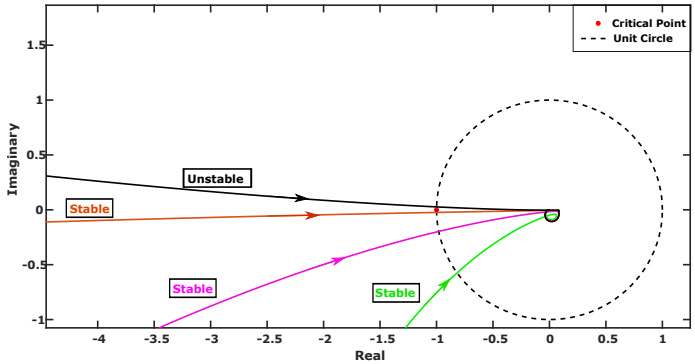

Figure 22. Nyquist Plot (evaluated at point P_1) at Low Power Level: Variation of DAB Gains on Stability.

The wind turbine control system has also been implemented in Simulink. The operation of the wind turbine has been studied both at start-up and at nominal power levels. Output voltage across C_{DC} is controlled to be at 5 kV. Figure 23 shows the output current of the WT system for two startup cases. Case I indicates the current response when the gains of DAB are reduced to a stable value represented by the green Nyquist curve in Figure 22. On the other hand, Case II (dark blue curve) represents the current response when the gains are increased, thereby increasing the system damping. This causes the settling time to reduce as can be observed here. One distinguishing observation between these two cases suggests that, as the gains are increased, the corresponding oscillations and settling time reduces. This result is also in coherence with the theoretical modelling of the system.

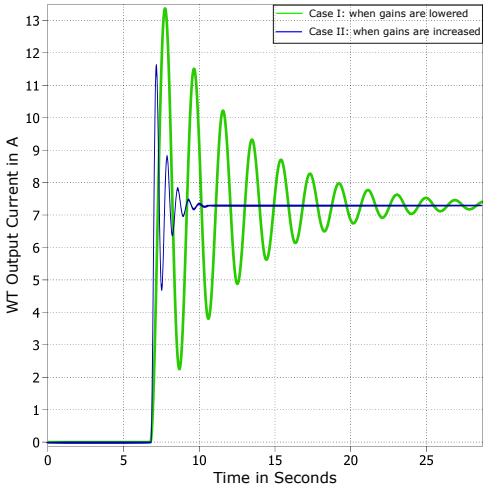

Figure 23. Simulink Verification—Effect of Variation of DC-DC Converter Gains on WT Output Current.

6.2. Star Configuration

Considering the star connected topology, the interesting nodes are at the output of the main WT (P_1), at star connection point (P_2) and at the input side of the DC/DC converter (P_3), which are illustrated in Figure 2. If the system is unstable at any of these nodes, it would imply that the system is unstable at other nodes unless passive notch filters are present which can block particular resonance frequencies. As an example, the stability results at the collector grid point P_3 are presented.

Consider a case with nine WTs in star configuration as shown in Figure 2. The stability is evaluated at DC/DC converter side (P_3). In this case, Z_s is the equivalent impedance of all the wind turbines together with submarine cables until point P_3 and Z_l is the impedance of the DC/DC converter. Up to eight WTs, the system is stable under nominal conditions and it has been observed that with nine WTs in star configuration under nominal conditions, the system tends to become unstable. This can be inferred from Figure 24 showing the frequency response and the Nyquist plot of this system.

From the high frequency response, the impedance ratio considered for evaluating stability is Z_l/Z_s. From the frequency response, it can be inferred that there is no RHP pole present for this impedance ratio. Now, for the system to be stable, there should not be any encirclement around the critical point in the Nyquist plot. However, the Nyquist plot of Z_l/Z_s (orange coloured plot in Figure 24) shows one clockwise encirclement.

It has been noted that such a system can be easily stabilized either by an active damping control or a passive damping control. In an active damping control, an increase in the gain of the DC/DC converter reduces the impedance of the DC/DC converter and results in a stiff collector grid. In a passive damping control, an increase of the WT output capacitance (C_{DC}) provides a low impedance path for disturbances. Figure 24 shows the stabilised system when the K_p gain of the DC/DC converter is increased. There is no encirclement observed in the Nyquist plot, and neither are there any RHP poles. This

shows that the system has been effectively stabilised. With more WTs, the star configuration can be operated stably by an active damping control by adjusting the gains of DC/DC converter. It should be noted that the closed loop pole locations for the increased gain are well within the bandwidth of the converter.

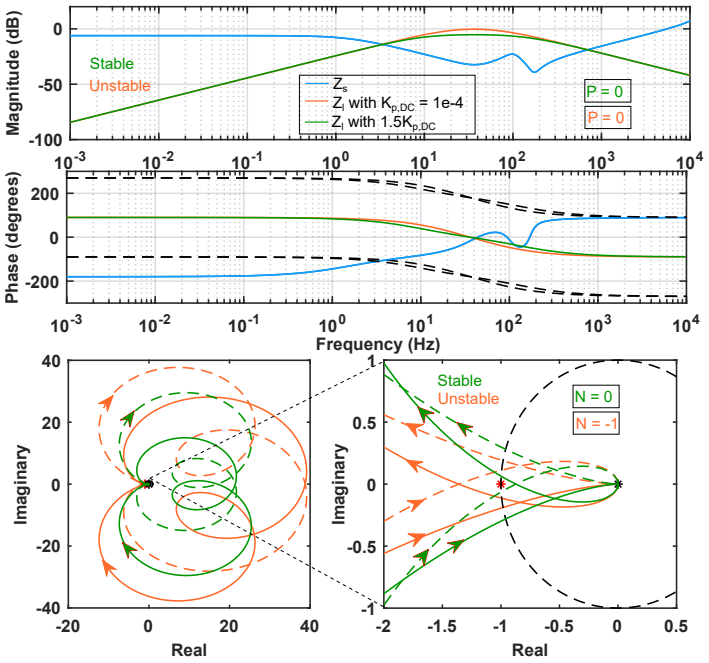

Figure 24. Star with 9 WTs—Impact of DC/DC converter proportional gain on system stability at P_3.

6.3. String Configuration

The string connections of WTs are shown in Figure 1 and the typical points of interest would be at the terminals of WT P_1 and at the collector grid P_3 as shown in Figure 1. For the considered system, more than eight WTs in the string leads to an unstable system. Figure 25 shows a case with nine WTs in the string connection under nominal conditions.

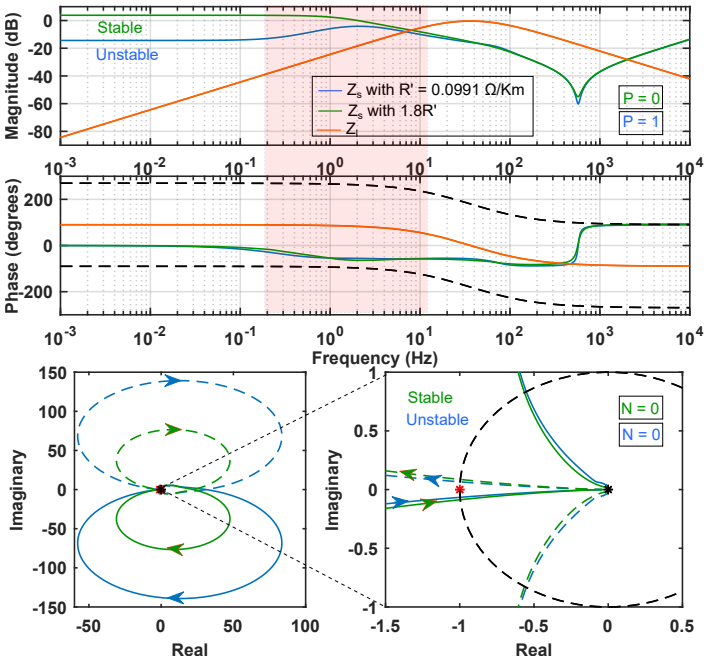

Figure 25. String with 9 WTs—Impact of cable resistance on system stability at P_3.

The stability has been evaluated at point P_3. Referring to Figure 25, from the frequency response of Z_s and Z_l, it can be deduced that the impedance ratio to be evaluated is Z_l/Z_s. Since there exists one RHP zero for Z_s, this means the impedance ratio Z_l/Z_s has one RHP pole. From the Nyquist plot, there are no encirclements around the critical point (red dot) indicating the presence of closed loop RHP poles, hence the system is unstable.

Due to the cascaded connection in the string, especially for longer strings, active damping control methods, such as WT and DC/DC converter control parameters, have a negligible effect on the stability since passivity is not preserved under parallel interconnection. In order to stabilise such system, the passive damping needs to be improved. If the submarine cable resistance is increased, the system ensured stability. In Figure 25, the orange curve shows the stabilised system frequency response and the Nyquist plot. As can be seen from the frequency response, the impedance ratio to be considered stays the same, that is, Z_l/Z_s. There is no RHP pole for this impedance ratio and neither are there any encirclements around the critical point, ensuring system stability.

7. Conclusions

This paper investigates the collector grid stability of DC offshore wind farms and performs a comparative study of star and string topologies on the aspect of stability. Small signal impedance models have been developed for wind turbines and DAB. Submarine cables cannot be modelled as transfer functions due to the presence of non-linear terms in the hyperbolic π model and therefore they are modelled as non-parametric impedance. An impedance building algorithm has been proposed to construct the non-parametric Thevenin equivalent impedance for complex systems, and stability analysis is performed using the non-parametric NSC. The stability of systems has been studied against the variation of WT, DC/DC converter control parameters, capacitance of WT and DC/DC converters and submarine cable parameters.

It can be concluded that the star arrangement is favourable compared to the string configuration w.r.t. stability, as the star point voltage is extremely stiff due to its proximity to the DC/DC converter, and the impedance of the DC/DC converter can be actively reduced to create a barrier for disturbances to circulate through the system. This was shown by varying the controller gains of the DC/DC converter and therefore varying the stiffness of the star voltage. Disturbances in the string configuration can distribute from one wind turbine to the next as the voltage is only stabilised by the DC/DC converter at one end. Here, the stability of the system could only be achieved via passive damping such as by increasing the resistance of the connecting cables, which of course is not favourable due to losses and there is no chance for adjustments after commissioning.

The accuracy of the proposed method depends on the correctness of the non-parametric impedance data points obtained from the measurement apparatus. A modified stability criterion needs to be formulated that takes into account the uncertainties of the measurement apparatus, which can be a future research work. Furthermore, the consideration of hybrid star-string topologies and optimum wind turbines per string from a stability viewpoint can also be a future extension of this work.

Author Contributions: Conceptualization, methodology, validation and writing, M.B., T.K. and S.K.G.; review and funding acquisition, F.P., A.M. All authors have read and agreed to the published version of the manuscript.

Funding: The frame of this research was partially funded by the German Federal Ministry for Economic Affairs and Energy (BMWI) within the project MuTiG 'Multi-Terminal intelligent/integrated Grids' (FK 0350007).

Institutional Review Board Statement: Not applicable

Informed Consent Statement: Not applicable.

Data Availability Statement: Not applicable.

Conflicts of Interest: The funders had no role in the design of the study; in the collection, analyses, or interpretation of data; in the writing of the manuscript, or in the decision to publish the results.

References

1. Lundberg, S. *Wind Farm Configuration and Energy Efficiency Studies-Series DC Versus AC Layouts*; Chalmers University of Technology: Gothenburg, Sweden, 2006.
2. Engel, S.P.; Stieneker, M.; Soltau, N.; Rabiee, S.; Stagge, H.; De Doncker, R.W. Comparison of the modular multilevel DC converter and the dual-active bridge converter for power conversion in HVDC and MVDC grids. *IEEE Trans. Power Electron.* **2014**, *30*, 124–137. [CrossRef]
3. Lakshmanan, P.; Liang, J.; Jenkins, N. Assessment of collection systems for HVDC connected offshore wind farms. *Electr. Power Syst. Res.* **2015**, *129*, 75–82. [CrossRef]
4. Wei, Q.; Wu, B.; Xu, D.; Zargari, N. Overview of offshore wind farm configurations. In *IOP Conference Series: Earth and Environmental Science*; IOP Publishing: Bristol, UK, 2017; Volume 93, p. 012009.
5. Bahirat, H.J.; Mork, B.A.; Høidalen, H.K. Comparison of wind farm topologies for offshore applications. In Proceedings of the 2012 IEEE Power and Energy Society General Meeting, San Diego, CA, USA, 22–26 July 2012; IEEE: Piscataway, NJ, USA, 2012; pp. 1–8.
6. Biskoping-ABB'Schweiz'AG. HVDC Circuit Breaker Switchyard. European EP3540750A1, 18 September 2019.
7. Khersonsky, Y.; Ericsen, T.; Bishop, P.; Amy, J.; Andrus, M.; Baldwin, T.; Bartolucci, B.; Benavides, N.; Boroyevich, D.; Chaudhary, A.; et al. *Recommended Practice for 1 to 35 kV Medium Voltage DC Power Systems on Ships*; IEEE: Piscataway, NJ, USA,2010.
8. Abeynayake, G.; Li, G.; Liang, J.; Cutululis, N.A. A Review on MVdc Collection Systems for High-Power Offshore Wind Farms. In Proceedings of the 2019 14th Conference on Industrial and Information Systems (ICIIS), Kandy, Sri Lanka, 18–20 December 2019; IEEE: Piscataway, NJ, USA, 2019; pp. 407–412.
9. Lyu, J.; Cai, X.; Molinas, M. Frequency domain stability analysis of MMC-based HVDC for wind farm integration. *IEEE J. Emerg. Sel. Top. Power Electron.* **2015**, *4*, 141–151. [CrossRef]
10. Amin, M.; Rygg, A.; Molinas, M. Self-synchronization of wind farm in an MMC-based HVDC system: A stability investigation. *IEEE Trans. Energy Convers.* **2017**, *32*, 458–470. [CrossRef]
11. Freijedo, F.D.; Rodriguez-Diaz, E.; Dujic, D. Stable and passive high-power dual active bridge converters interfacing MVDC grids. *IEEE Trans. Ind. Electron.* **2018**, *65*, 9561–9570. [CrossRef]
12. Liu, B.; Li, Z.; Zhang, X.; Dong, X.; Liu, X. Impedance-Based Analysis of Control Interactions in Weak-Grid-Tied PMSG Wind Turbines. *IEEE J. Emerg. Sel. Top. Circuits Syst.* **2020**, *11*, 90–98. [CrossRef]
13. Zhou, W.; Wang, Y.; Chen, Z. Reduced-order modelling method of grid-connected inverter with long transmission cable. In Proceedings of the IECON 2018-44th Annual Conference of the IEEE Industrial Electronics Society, Washington, DC, USA, 21–23 October 2018; IEEE: Piscataway, NJ, USA, 2018; pp. 4383–4389.
14. Sun, J. Impedance-based stability criterion for grid-connected inverters. *IEEE Trans. Power Electron.* **2011**, *26*, 3075–3078. [CrossRef]
15. Riccobono, A.; Santi, E. Comprehensive review of stability criteria for DC power distribution systems. *IEEE Trans. Ind. Appl.* **2014**, *50*, 3525–3535. [CrossRef]
16. Gurumurthy, S.K.; Uhl, R.; Pitz, M.; Ponci, F.; Monti, A. Non-Invasive Wideband-frequency Grid Impedance Measurement Device. In Proceedings of the 2019 IEEE 10th International Workshop on Applied Measurements for Power Systems (AMPS), Aachen, Germany, 25–27 September 2019; IEEE: Piscataway, NJ, USA, 2019; pp. 1–6.
17. Monti, A.; Gurumurthy, S.K.; Uhl, R.; Pitz, M. Vorrichtung zur Bestimmung der Impedanz in Abhängigkeit der Frequenz eines zu messenden Versorgungsnetzes. Patent DE 102019214533, 25 March 2021.
18. Liao, Y.; Wang, X. Impedance-based stability analysis for interconnected converter systems with open-loop RHP poles. *IEEE Trans. Power Electron.* **2019**, *35*, 4388–4397. [CrossRef]
19. Liu, X.; Islam, S. Reliability issues of offshore wind farm topology. In Proceedings of the 10th International Conference on Probablistic Methods Applied to Power Systems, Rincon, PR, USA, 25–29 May 2008; IEEE: Piscataway, NJ, USA, 2008; pp. 1–5.
20. Zarkov, Z.; Demirkov, B. Power control of PMSG for wind turbine using maximum torque per ampere strategy. In Proceedings of the 2017 15th International Conference on Electrical Machines, Drives and Power Systems (ELMA), Sofia, Bulgaria, 1–3 June 2017; IEEE: Piscataway, NJ, USA, 2017; pp. 292–297.
21. Doncker, R.W.D. *Advanced Electrical Drives: Analysis, Modeling, Control*; Springer: Berlin, Germany, 2011.
22. Cupelli, M.; Gurumurthy, S.K.; Bhanderi, S.K.; Yang, Z.; Joebges, P.; Monti, A.; De Doncker, R.W. Port controlled Hamiltonian modeling and IDA-PBC control of dual active bridge converters for DC microgrids. *IEEE Trans. Ind. Electron.* **2019**, *66*, 9065–9075. [CrossRef]